Theor. Comput. Fluid Dyn.
https://doi.org/10.1007/s00162-023-00647-0

ORIGINAL ARTICLE

Al Shahriar · Rajan Kumar · Kourosh Shoele

Vortex dynamics of axisymmetric cones at high angles of attack

Received: 31 January 2023 / Accepted: 29 March 2023

Abstract Vortex asymmetry, dynamics, and breakdown in the wake of an axisymmetric cone have been investigated using direct numerical simulation for a wide range of angles of attack. The immersed boundary method is employed with pseudo-body-conformal grids to ensure the accuracy and resolution requirements near the body while being able to account for topology changes near the cone tip. The separated shear layer originated from the surface of the cone swirls into a strong primary vortex. Beneath the primary vortex on the leeward surface of the cone, a well-coherent counter-rotating secondary vorticity is generated. Beyond a particular threshold of swirl, the attached vortex structure breaks and the flow undergoes a chaotic transformation. Depending on the angle of attack, the flow shows different levels of instabilities and the topology of the vortices changes in the wake. In addition to swirl, spiral vortices that revolve around the primary vortex core often merge with the core and play a role in developing the double-helix mode of instability at the onset of the vortex breakdown. At the angle of attack of 60°, the time-averaged side force becomes asymmetric at the stage where the drag overcomes the lift. At the angle of attack of 75°, the primary vortex governs the flow asymmetry and the side force. Flow asymmetry is independent of the vortex breakdown. Finally, the contribution of primary vortices to the total forces is quantified using a force partitioning method.

Keywords Symmetry breaking · Vortex breakdown · Direct numerical simulation (DNS) · Axisymmetric forebody · Force partitioning method

1 Introduction

Three basic phenomena that characterize the flow over bodies of revolution/axisymmetric bodies (e.g., a cone) are the dynamics of primary and secondary vorticity [1–3], vortex breakdown [4–9], and flow asymmetry [10–12]. Both from the perspective of understanding the fundamentals of aerodynamics and practical applications, flow over an axisymmetric body and the effect of the angle of attack (AoA) have been studied for an extended period of time [6,7,13]. Flow over an axisymmetric body at high AoA is associated with a separated shear layer, which eventually leads to the roll-up of the concentrated vortices and formation of the primary vortex structures (often have an axisymmetric conical/cylindrical shape) [13,14]. Because of freestream flow entrainment created by the primary vortices, the secondary reverse flow develops on the leeward side of the axisymmetric body. This reversed flow can undergo separation on the leeward side of the cone surface, which is known as the secondary separation and the associated vorticity is known as the secondary vorticity [11]. The characteristics of the secondary vorticity are governed by the effective Reynolds number of the boundary layer generated by

Communicated by Vassilis Theofilis.

A. Shahriar · R. Kumar · K. Shoele (✉)
Department of Mechanical Engineering, FAMU-FSU College of Engineering, 2525 Pottsdamer St., Tallahassee, FL 32310, USA
E-mail: kshoele@eng.famu.fsu.edu

Published online: 04 May 2023

the secondary flow. Based on AoA and Reynolds number, the primary and secondary vortices can be unsteady and exhibit nonlinear instabilities. The primary separated shear layer (the vortex sheet) may contain smaller concentrated vortices, which are referred to as "vortical substructure" [1,3].

Significant similarities exist between the flow fields over the delta wing and the axisymmetric cone. The major exception is that for the delta wing, the primary vortex starts to curl from highly swept and sharp leading edges of the wing [3,15–17], whereas, for an axisymmetric cone, the separation occurs over the smooth curved surface and the zone between primary and secondary separation is comparatively larger. For flow over an axisymmetric body, the vortex separation onset relates to the separating shear layer from a smooth cylinder/ellipse cross section, reminiscent of the flow over a circular bluff body. This induces the primary wake instability, known to be the result of a Hopf bifurcation, scaling with the diameter of the bluff body [18]. In addition, the separated flow experiences shear-layer instabilities driven by the Kelvin–Helmholtz mechanism over the thickness of the separating shear layer. In contrast, there is a separation at the edge for flow over the delta wing, and the subsequent flow modifications are only associated with the shear-layer instability driven [19]. The presence of both mechanisms in axisymmetric geometries creates a more complex vortex interaction and wake structure and results in a higher tendency for the wake to become asymmetric.

A higher angle of attack and Reynolds number lead to a higher degree of swirl or circulation in the primary vortex, which results in breaking the primary vortex into smaller rotational elements at some distance along the axis of the vortex. This phenomenon, characterized by rapid changes in the axial direction, is referred to as "vortex breakdown" and usually takes place in two forms: (1) formation of axisymmetric/bubble-type vortical structures and (2) formation of spiral/helical vortical structures; [4–7,17,20]. It is often postulated that the helical form of vortex breakdown is a consequence of the instability of the bubble type breakdown [8,16,20]. Looking at the time-averaged mean flow field, the vortex breakdown can be noticed as a rapid decrease of both the axial and swirl components of velocity and a dramatic expansion of the vortex core [1]. The vortex breakdown leads to a drop in the lift force and pitching moment and could drive unsteady buffeting of the body [3]. If the angle of attack increases, the distance between the onset location of the breakdown and the apex of the conical vortex decreases [21]. Escudier identified Reynolds number (Re), swirl number/parameter (defined as $\Omega = \Gamma/LU$, where L and U are the corresponding length and velocity scales), and swirling ratio (radial-to-tangential velocity ratio) [8] as the major parameters for providing a global description of the flow and showed that the onset of vortex breakdown was strongly correlated with these characteristic parameters.

The pair of primary vortices often shows asymmetry in the wake of an axisymmetric body at high AoA [22,23]. The flow asymmetry results in unpredictable side forces and yawing moments on the body. Small imperfections near the apex of the body can cause vortex asymmetry and flow instabilities even at small AoAs [12,24–26] where the initiation and growth of asymmetry in the vortices strongly correlate with the relative size and shape of the imperfections, e.g., ratio of imperfection height to the local boundary-layer thickness [11,25,27,28]. Zhu et al. [29] observed asymmetry in the vorticity and side forces even before any apparent asymmetry in the primary separation. They concluded that the asymmetric shear layers, generated due to asymmetric boundary layer disturbances created by artificial micro-imperfection, are continuously fed into the primary vortex, which eventually causes flow asymmetry. When micro-imperfections are located on the windward side, it delays the separation. On the other hand, leeward side imperfections promote the separation/vortex roll-up [30]. Levy et al. identified the flow asymmetry as a convective instability by analyzing the correlation between the imperfections near the apex and the asymmetric flow [31]. The symmetry breaking on the axisymmetric body has many similarities to the asymmetric flow over the delta wing as well [32]. In addition to the small surface perturbation, "hydrodynamic instability" resulting from the "crowding" together of the vortices is also a common factor for the asymmetric response of both the slender axisymmetric body and delta wing [33]. For flow over a delta wing, vortex asymmetry was seen on the time-averaged results for higher values of the similarity parameter ($K = \tan\alpha/\tan(90^\circ - \Lambda)$, where α and Λ are the AoA and sweep angle, respectively) [3]. It was shown that the vortex asymmetry is independent of the vortex breakdown [3]. At high AoA, the hydrodynamic instability is the main reason behind the asymmetric wake. It was previously shown that the only source of the side-force asymmetry could be the flow structure around the forebody of an axisymmetric object with both forebody and afterbody arrangements, such as a cone-cylinder or ogive-cylinder [34]. It has been observed that the side vortex force can exceed the normal force acting on a slender axisymmetric body [35].

The separated shear layer dynamics and secondary vorticity are other significant factors that characterize these flow fields. Separated shear layers have been found to exhibit discrete vortical substructures [1,36,37]. The secondary separation undergoes a process of eruption and shedding [2,38]. Later, these packets of secondary vorticity interact with the separated shear layer and divide it into segments. This strong interaction creates a

zone of alternative negative and positive vorticity. A similar mechanism has been observed by Visbal et al. [38], who identified an unsteady substructure on the separated shear layer. The suction in the secondary separation suppresses the substructures and diminishes the shear-layer instability. This instability also diminishes at low Reynolds numbers. These substructures have the tendency to be both spatially stationary (spatially fixed around the outskirts of the primary vortex) [39,40] and temporally varying (spinning around the primary vortex) [1,38]. One hypothesis is that the substructures are developed by the mechanism responsible for the Kelvin–Helmholtz instability [39,41]. Another hypothesis suggests that the substructures originate from transversal perturbations along the leading edge of the wing induced by the interaction between the separating shear layer and the secondary vorticity [38,40]. The substructures also undergo severe straining, deformation, and breakups which eventually cause the transition of the separated shear layer [37,42].

Nevertheless, the causal mechanisms of the formation of asymmetric flow over an axisymmetric body at higher AoA still need to be better understood. The influence of secondary vorticity on vortex breakdown and symmetry breaking has yet to be thoroughly studied. The cone, the most canonical axisymmetric shape, is a perfect choice to study these effects. The flow structure over the cone progresses through different stages in a self-similar fashion since the cone surface lacks a specific geometrical length scale that uniquely scales the wake flow field. Instead, the formation of vortices and the growth of the boundary layer highly depend on the geometry (cone angle) and the intrinsic length scale of the cone cross section parallel to the flow direction. In this paper, we extend our previous study [43] and explore the role of AoA on vortex formation, breakdown, and symmetry breaking. The study's primary objective is to find potential characteristic parameters that encompass the geometrical and flow dynamical aspects of the problem. The transition location and post-transition aerodynamics of self-similar coherent structures are identified using such metrics (Fig. 1).

2 Numerical technique

2.1 Flow solver

The governing Navier–Stokes equations are solved using direct numerical simulations (DNS) on curvilinear staggered grids with the immersed boundary method [44,45]. The transformed unsteady incompressible governing equations can be evaluated for the chosen Eulerian generalized coordinate system (ξ_1, ξ_2, ξ_3) as:

$$\frac{\partial U^i}{\partial \xi_i} = 0, \tag{1}$$

$$\frac{\partial (J^{-1} u_i)}{\partial t} + \frac{\partial F_{ij}}{\partial \xi_j} = 0, \tag{2}$$

where F_{ij} is the total flux defined as

$$F_{ij} = U_j u_i + J^{-1} \frac{\partial \xi_j}{\partial x_i} p - \frac{1}{Re} G^{jk} \frac{\partial u_i}{\partial \xi_k}. \tag{3}$$

Here, x_i, u_i, p and Re denote the Cartesian coordinates, velocity, pressure, and Reynolds number, respectively. J^{-1} is the inverse of Jacobian, $\mathbf{J}$, or the volume of the cell. The Jacobian $\mathbf{J}$ is the geometric property of the transformation from the Cartesian coordinate and the curvilinear coordinate, $x_1, x_2, x_3 \rightarrow \xi_1, \xi_2, \xi_3$ and is defined as $\mathbf{J} = \partial(\xi_1, \xi_2, \xi_3)/\partial(x_1, x_2, x_3)$. Here, $U_i = J^{-1}(\partial \xi_i / \partial x_j) u_j$ is the volume flux or the contravariant velocity scaled by J^{-1} normal to the surface with constant ξ_i and $G^{ij} = J^{-1}(\partial \xi_i / \partial x_k)(\partial \xi_j / \partial x_k)$ is the "mesh skewness tensor."

Here, a second-order accurate fractional step method and a central difference method are employed to discretize the governing equations [46]. The Poisson equation is solved with an iterative solver with the geometrical multigrid preconditioner. A staggered grid is employed, wherein the pressure is defined at the control volume's centers, and the velocity components are defined at the face centers to strongly enforce mass for each grid cell.

In particular, intermediate volume fluxes are calculated at the surface centers and used to calculate the pressure that satisfies the continuity equation in the projection step. To enhance the numerical stability, a matrix-free Newton–Krylov method is used for solving the momentum equations [47]. A detailed description of the numerical method can be found in [44].

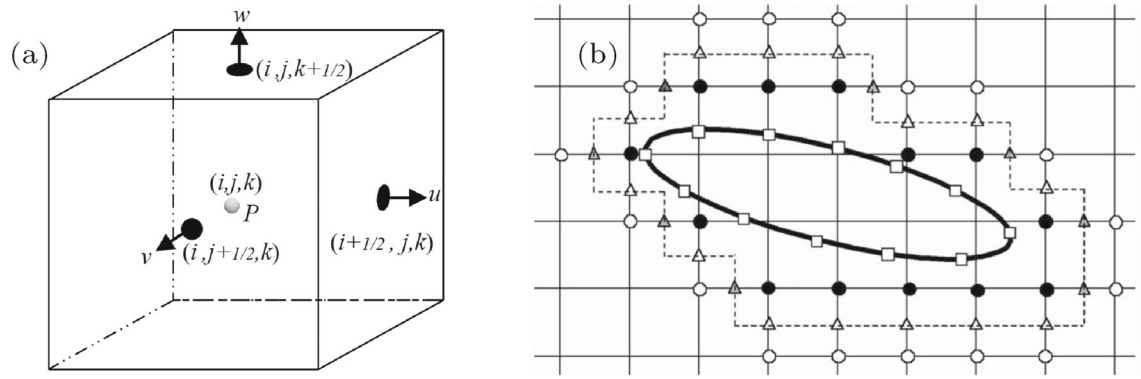

Fig. 1 **a** Indexing of volume center (i, j, k) and surface centers. **b** Representation of the sharp-interface immersed boundary method. Open square: Lagrangian immersed boundary grid points; filled circle: immersed boundary nodes; triangle: boundary nodes of the staggered grid points (filled and open triangles indicate u and v velocity); open circle: the last layer of nodes where the discrete continuity equation is applied [45]

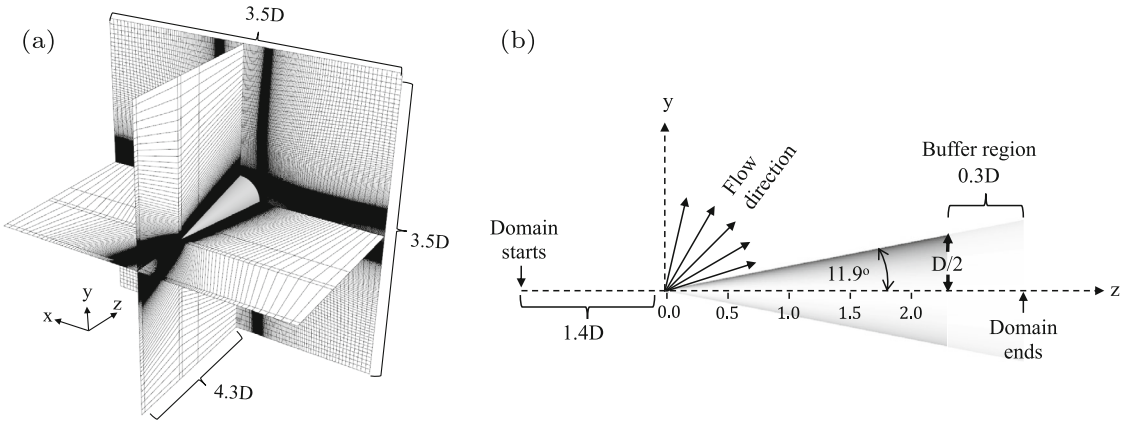

Fig. 2 **a** Curvilinear grid and the physical domain. Specific grid points were selected to illustrate the computational mesh in the physical domain (D is the base diameter of the cone). **b** Schematic of the cone with flow direction and dimensions

The sharp interface curvilinear immersed boundary method framework is used to represent the cone structure in the Eulerian flow domain. The axisymmetric body is identified by unstructured triangular surface meshes where the no-slip wall boundary conditions are enforced [45]. One potential technique to implement a sharp-interface immersed boundary method is to extrapolate the values at the ghost cell inside the solid domain to discretely satisfy the kinematic boundary conditions [48–50]. In another approach, the kinematic conditions are interpolated from the surface to the closest Eulerian grid points in the fluid domain based on the minimum distance from the fluid-solid interface [45]. The latter approach is adopted in the present study to impose flow boundary conditions to the second order on the body at every instant in time.

2.2 Curvilinear semi-conformal grid generation

To improve the accuracy of the numerical solution of the field variables, finer grids are provided close to the body surface. The curvilinear grids are semi-conformal to the surface of the body except for the zone close to the apex of the cone. Typical non-uniform Cartesian grids on xy-plane pass through a specific transformation to conform to the surface of the cone based on the cross-sectional diameter along the z-direction. The distance between grid points near the surface gradually decreases along the cone's axis, while the grid points far from the surface adjust their position accordingly. A schematic of the grid arrangement (selected grid lines) is shown in Fig. 2a on three planes perpendicular to the coordinate axis.

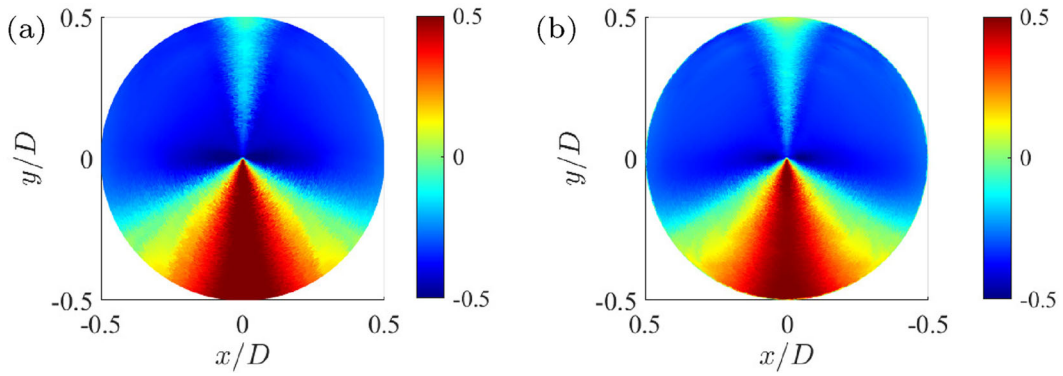

Fig. 3 Instantaneous pressure on the surface for AoA = 45° with **a** base grid selected for the current study and **b** refined grid

2.3 Simulation parameters

Numerical simulations were conducted for flow over a conical shape with a fluid domain where the cone's centerline is aligned with the Eulerian z-axis as depicted in Fig. 2b. The half-angle of the cone is fixed at 11.9°. These geometrical parameters are selected from the experiments reported in [51]. The number of grid points in each spatial direction is $227 \times 301 \times 540$. The domain size in the direction of the cone axis is $4.3D$, including the buffer region with a thickness of $0.3D$ near the outflow. The cone's diameter at the interface of the main domain and buffer domain is used as the characteristic length in this study and is denoted as D. This choice allows a consistent comparison between different AoA cases despite the fact that the flow is developing both in the circumferential and axial directions on the surface of the cone. The computational domain is extended to $1.4D$ from the cone tip to the inflow boundary condition. To avoid the effect of the outflow boundary condition, the results are only processed for the net computational domain of $3.5D \times 3.5D \times 2.6D$. The numerical parameters are checked to ensure that simulation results are grid-converged and are domain size independent.

In the rest of the paper, the Reynolds number ($\mathrm{Re_D}$) based on the base diameter (D) of the cone is set at 3500. As a sample test conducted to determine the convergence of the solution, simulation has been performed for AoA $= 45°$ with $453 \times 601 \times 504$ grid points. The maximum pressure at the base of the cone and the windward side is 0.48 $(P - P_\infty)/\rho U_\infty^2$, within 5% of the results obtained for the selected grid. The sample instantaneous surface pressure fields from both grids are shown in Fig. 3. The averaging time (tU_∞/D) for AoA $= 45$, 60, and 75° is 8.0, 14.5, and 21.5, respectively. After passing the transient phase, the time-averaged surface pressure data was collected with a time interval of $0.057(tU_\infty/D)$ between each snapshot.

3 Results

Fully resolved flow simulations are done for the cross-flow over a cone at AoA of 0°, 15°, 30°, 45°, 60° 75°. At AoA $= 0°$, the flow is completely steady for the chosen Reynolds number, and the flow is fully attached with no vortex separation. Hence, the results of this case have not been discussed in the study. Similarly, for AoA $= 15°$, the flow field in the wake does not have well-defined structures in the wake, e.g., a clear roll-up of primary vorticity and the presence of secondary vorticity. Because of this reason, some of the vortex dissection analyses were not executed for this case. On the other limit, the highest limit of AoA of 75° is selected since, at this AoA, the flow possesses all the necessary features on which this study focuses, including the asymmetric side force and vortex breakdown. For the low AoA range, the flow predominantly develops in the axial direction with weak primary vortices in the wake. As the AoA increases, the flow topology adjusts, and the boundary layer develops in the circumferential direction. The geometrical effect now drives the separating shear layer to roll and create stronger primary coherent vortex structures on the leeward side. The geometry of the cone (mainly the cone angle) and the AoA are both important factors that specify the wake structure and are responsible for the relative importance of the cross and longitudinal flow features.

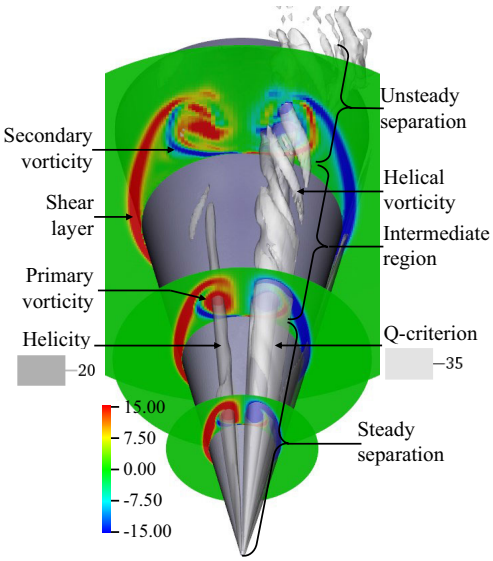

Fig. 4 Isosurface of the Q-criterion (light gray isosurface in the right half of the figure) and helicity (dark gray isosurface in the left half) of the instantaneous flow field for AoA $= 45°$. Contour slices showing the z-component of instantaneous vorticity (ω_z) at $z/D \approx 0.5$, 1.4, and 2.25

3.1 Vortex dynamics of the wake and large flow coherent structures

An example instantaneous flow field for AoA $= 45°$ is displayed in Fig. 4. The flow is associated with primary (the red region on the left of the contour slices) and secondary (the blue region attached to the cone surface) vortical structures in the wake, as indicated in Fig. 4. The boundary layer develops both in the circumferential direction from the windward side and in the longitudinal direction progressively from the tip of the cone. The favorable pressure gradient on the windward side of the cone helps to suppress any shear instabilities up to the separation point [52]. Once the boundary layer reaches the leeward side of the cone and the adverse pressure gradient becomes dominant, the boundary layer separates from the body. This separated concentration of vorticity swirls into the coherent primary vortex structure. No shear layer instabilities are observed at this AoA. The size of the primary vortex grows along the axial direction. Near the tip of the cone, the primary vortices remain coherent and steady, along with a strong counter-rotating secondary vorticity.

On the leeward side, because of the swirling primary vortex and adverse pressure gradient, a strong near-body reverse flow emerges. This reverse flow has the vorticity component with the principal axes in the direction opposite to the primary vortex, identified in the average z-vorticity (ω_z) isosurface in Fig. 4. The secondary flow also separates from the surface, and this separation is known as a secondary separation. The directions of the rotation of the primary and secondary vorticity are opposite; therefore, the near-body secondary vorticity results in the lift of the primary vortices from the cone surfaces. Once the secondary flow is separated, it curls around the primary vortex and is then entrained into the primary vortex. Compared with the flow over the delta wing, the interaction zone between primary separation and secondary separation is wider in Fig. 5. From the tip to $z/D \approx 1.1$, both separations happen almost at the same polar angle ($\theta \approx 45$). After $z/D \approx 1.1$ along the axial direction, the primary and secondary separations occur at different polar angles, and the angular gap between the primary and secondary separation widens along the axial direction. In the zone between primary and secondary separations, the near-wall velocity vector has an axial component in the opposite direction of flow on the windward side of the cone. Consequently, the interaction of the secondary vorticity with the incoming separated shear layer is delayed for flow over a cone. The shape of the secondary vorticity region changes gradually in the axial direction from a slightly flat shape to a semi-circular shape. The center of the primary and secondary vorticity is shown by the 3D curve in Fig. 6. In the appendix, a description has been provided regarding the procedure to obtain the zone occupied by primary and secondary vorticity. The curve color represents the circulation around the primary and secondary vorticity on the xy-plane.

Another relatively small-scale vortex in the shape of a helix develops around the primary vortex. These vortices can be identified in the isosurface of the Q-criterion shown in the right part of Fig. 4 in the intermediate region. The phrase "helical vortex" will be used here to refer to this separate and distinctly different coherent

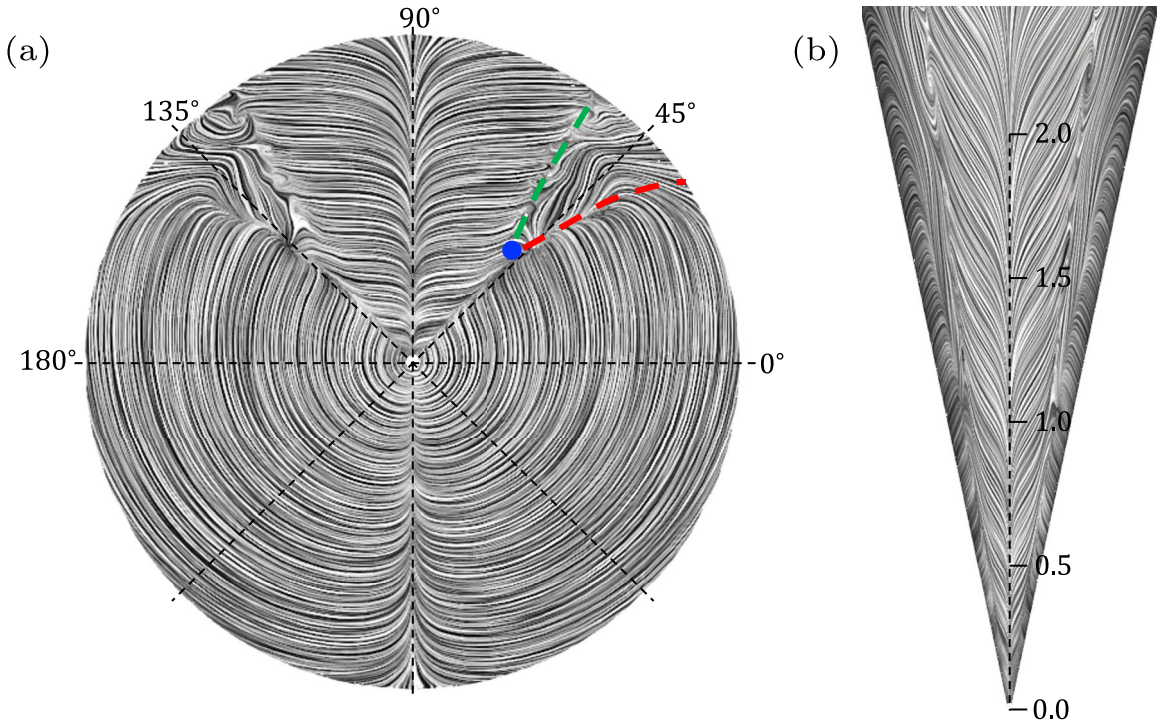

Fig. 5 Limit surface streamlines for AoA = 45° for view angle perpendicular to **a** front view (xy plane) and **b** top view (xz plane). The red and green dashed line shows the primary and secondary separation locations, respectively. The blue dot shows the location where the primary and secondary separation started to diverge (color figure online)

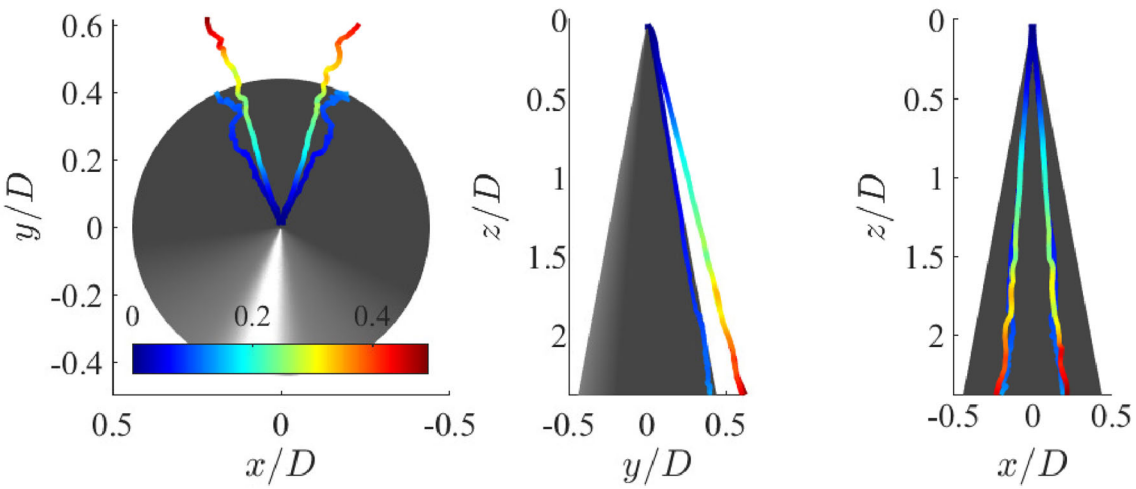

Fig. 6 The color of the 3D curves shows the magnitude of circulation around the primary and secondary vorticity. For the primary vortex, the 3D curve is positioned at the center of the statistically determined core of the vortex. For the secondary vorticity, the line is at the centroid of the secondary vorticity (color figure online)

structure. In the literature, these vortices are often called "substructures." The helical vortices are three-dimensional, stable, and deform in a helical shape around the primary vortex originating from the interaction zone between primary and secondary separation. The three-dimensional reconfiguration of the secondary and helical vorticity accounts for the irregularity of the conical shape of the primary vortex. At a low angle of attack, this connection is weakened since the geometrical aspect has a constructive role in keeping the primary vortex stabilized. The helical vortices are generated inside the zone between primary and secondary separation and, later, interact with the separated shear layers after a partial spiral revolution. Once the helical vortex

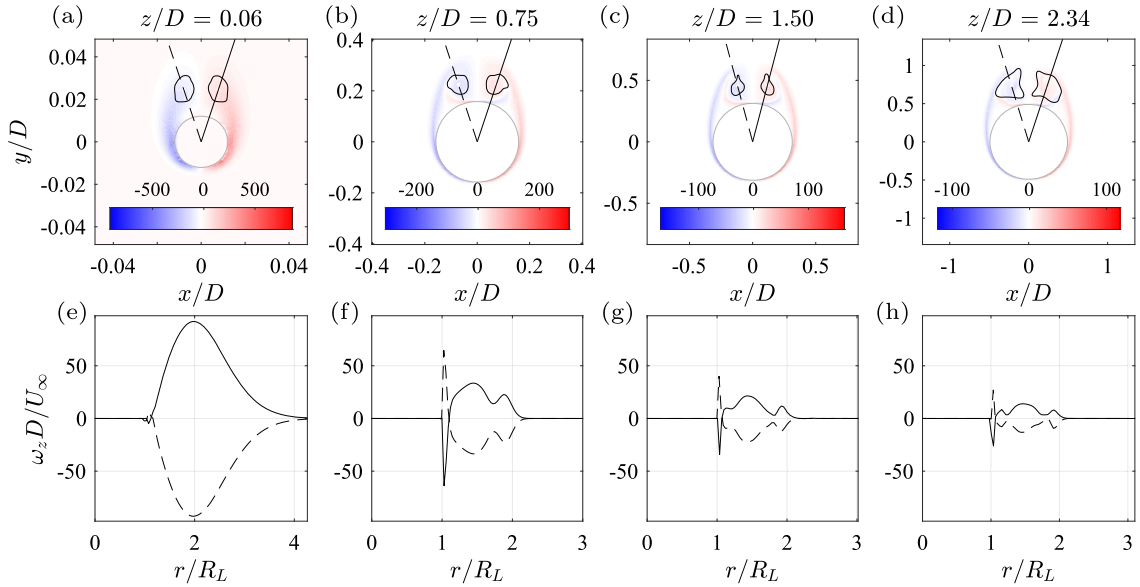

Fig. 7 Contour slices of the z-component of the vorticity at $z/D \approx$ **a** 0.06, **b** 0.75, **c** 1.5, and **d** 2.3 for AoA $= 45°$. The black closed path shows the zone for the primary vortex. **e**–**h** vorticity along the line drawn in the contour slices on the top row. The line is drawn from the center of the cone to the center of the primary vortex

starts interacting with the separated shear layer, it undergoes severe straining. It was postulated that these helical vertices are associated with secondary instabilities which clarify the fact that stationary and unsteady substructures in the separated shear layer are two different representations of the same phenomenon [53]. The surface streamlines, shown in Fig. 5, delineate the zone between the primary and secondary separations and close observation of the instantaneous Q-criterion (Fig. 4) shows that the helical vortices originated mostly from this zone.

For AoA $= 45°$, the vorticity slices on the xy-plane at different z/D locations are shown in Fig. 7. At $z/D \approx 0.06$, both the primary and secondary vorticity are first visible in Fig. 7a where the separated shear layer has not been able to curl into a well-defined primary vortex core and the thickness of secondary vorticity is very small. At a larger z/D distance from the tip, the primary separated shear layers curl into a well-defined vortex pair. Simultaneously, the secondary flow also grows underneath the primary vortex. Fig. 7e–h shows the z-component of the vorticity along the line that connects the center of the cone and the primary vortex for the corresponding slice on the top row. The plots show the relative variation in primary and secondary vorticity, size of the primary vortex, and thickness of the secondary flow for different z/D.

The results suggest that the wake behind a cone at higher AoA can be divided into three main regions: steady (consisting of primary and secondary vorticity only), intermediate (contains both primary and helical vortex), and unsteady region (small-scale irregular vortical structures). Helicity is found to be a suitable indicator of the coherent vortex core by separating it from the vortex sheets, which can be noticed in the vorticity contour plots. The flow is essentially steady up to the local Reynolds number (Re_{D_L}) of approximately 1750, where D_L is the diameter of the cone at L distance from the tip. Up to this distance from the tip, the Q-criterion in Fig. 4 shows a strong and stable vortex core and the wake poses complete symmetry. From Re_{D_L} of 1750 to approximately 2900, an intermediate region emerges where the flow is predominantly steady and the core of the vortex is accompanied by the surrounding coherent helical vortices. Beyond the Re_{D_L} of 3300, the separated shear layer, primary vortex, helical vortices, and secondary separation show significant unsteadiness. At a high angle of attack (AoA $= 60$ and $75°$), this zone is associated with vortex breakdown. The separated part of the secondary flow shows unsteady behavior, while the attached part of the secondary flow stays steady.

3.2 Effect of the angle of attack

In this section, we investigate the effect of AoA on the flow over a cone and the vortical structure in the wake. The Reynolds number (Re_D) is fixed at 3500 for the rest of the discussion in this section.

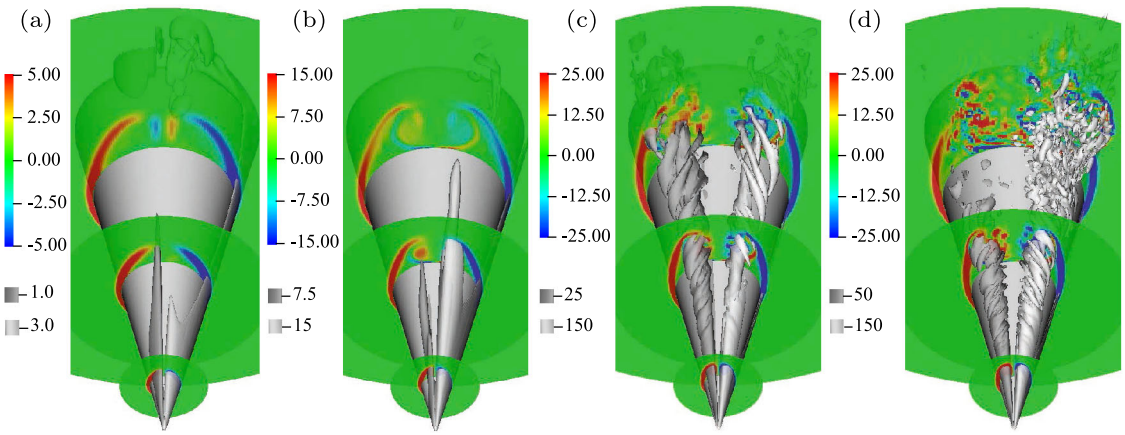

Fig. 8 Instantaneous flow fields for AoA = **a** 15°, **b** 30°, **c** 60° and **d** 75°. For caption, see Fig. 4

3.2.1 Effects on the vortical coherent structures

At a low AoA of 15°, the wake is only associated with the partial roll-up of the separated shear layer as shown in Fig. 8a. Both primary and secondary vortices can be seen in Fig. 8b for AoA of 30°. No helical vortex was observed in these two AoA cases. At AoA = 45°, 60° and 75°, shown in Figs. 4 and 8c, d, a similar response is observed near the tip. In terms of the unsteady behaviors, the characteristics of the flow field in this study match the classification by Degani [34] for flow over the slender ogive-cylinder body: (1) steady (AoA < 40°), (2) transitional (40° < AoA < 60°), and (3) non-stationary (AoA > 60°).

For AoA = 60 and 75°, at some distance from the tip in the axial direction, the strong primary vortex core cannot maintain its coherent shape. The core of the primary vortex breaks into small-scale vortical elements. The wake no longer has the predictable configuration of the primary, secondary, and helical vorticity. The reported phenomenon of ejection of concentration of secondary vorticity [2,53,54] is observed after the vortex breakdown.

To investigate the impact of helical vorticity on the vortex breakdown, the instantaneous flow field before and after the location of vortex breakdown is closely inspected in Fig. 9. At first, four helical vortices are identified (HV1, HV2, HV3, and HV4) that revolve around the primary vortex core (Fig. 9a). Two more images of the isosurface are also shown in Fig. 9b, c (view from the $+x$ and $-x$ directions) for a better visual representation of the 3D configuration of the vortices. On the first slice in Fig. 9d, the same vortices are identified again. The helical vortex HV1 is very close to the core of the vortex. On the second slice at $z/D \approx 0.86$, HV1 shifts closer to the core. HV2 and HV3 attain a new position after a slight revolution around the core. In the next downstream location shown in Fig. 9f, HV1 merges with the core and HV2 moves closer to the core. However, unlike the helical vortices HV1 and HV2, the third helical vortex (HV3) moves away from the vortex core and becomes weaker. In the next slice at $z/D \approx 0.98$, significant topological changes have been noticed, and this point can be considered as the location of the vortex breakdown. At this stage on slice-4 in Fig. 9g, no distinct core of the primary vortex can be identified; instead, two new vortices (DH1 and DH2) are observed, which can be considered as the representation of the double helix mode of vortex breakdown as described in [20]. While HV1 merges with one part of the double helix (DH2), HV3 becomes weaker, undergoes severe straining, and almost diminishes at this stage. A sharp rise in pressure and a drop in vorticity were observed at the same location. In the later stage at $z/D \approx 1.05$, the double helix sustained its shape, and the generation of new vortical elements is noticed. Downstream of this point, the flow becomes chaotic and shows wake-like behaviors.

The location of vortex breakdown obtained by inspecting the average flow field is given in Table 1. The vortex breakdown location is identified by a steep rise in the average turbulent kinetic energy (TKE) at the core of the vortex, shown in Fig. 10. At $z/D \approx 2.1$, a sharp rise has been observed in TKE in Fig. 10a for both the left and right vortex. For AoA = 75°, asymmetric vortex breakdown (sharp rise in TKE) at $z/D \approx 0.9$ and $z/D \approx 1.1$ is noticed. As the flow experiences a higher degree of swirl at higher AoA, the vortex breakdown occurs earlier (similar behavior reported in Ref. [21]).

In Table 1, the axial-averaged polar angle (θ) of the center of the primary vortex is documented. The difference between the polar angle of the left and right primary vortex center also increases as the AoA

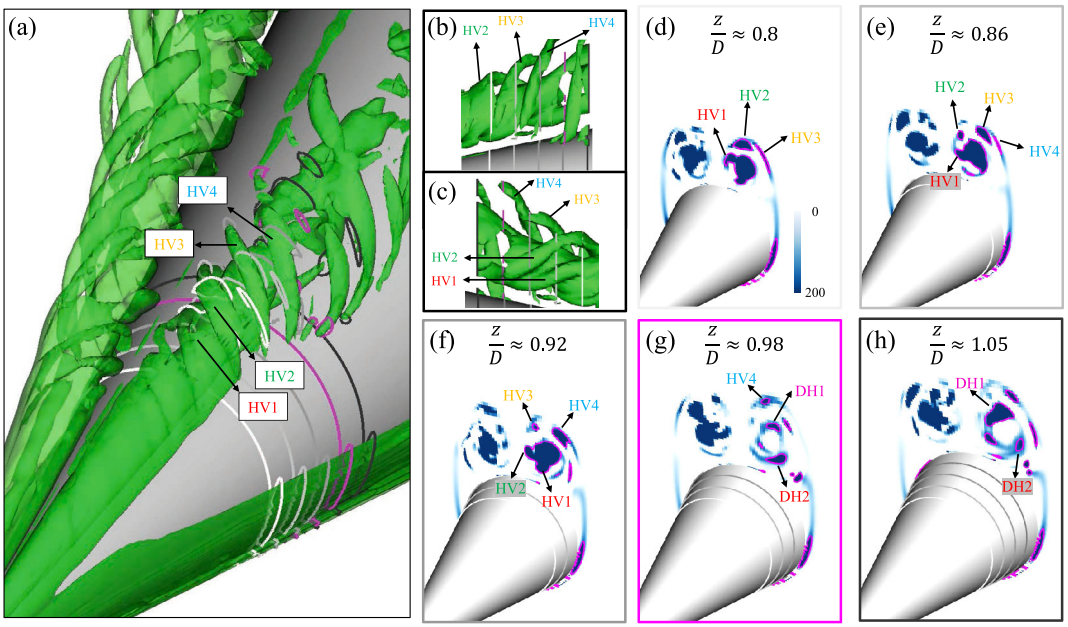

Fig. 9 Isosurface of Q-criterion: **a** isometric view; **b** and **c** side view from $+x$ and $-x$ direction, respectively. **d**–**h** Contour slices of Q-criterion at different z/D locations before and after the vortex breakdown for AoA $= 75°$. Abbreviations: helical vortex (HV), double helix (DH). The locations of the slices are shown by the corresponding outline color in the isosurface images

Table 1 Effects of AoA on vortex core location and breakdown location (z_{vb}/D)

Type	Vortex	Angle of attack				
		15°	30°	45°	60°	75°
z_{vb}/D	Left	–	–	–	2.1	0.9
	Right	–	–	–	2.1	1.1
$\langle\theta\rangle$	Left	–	74.69	74.00	72.81	71.10
	Right	–	74.68	74.03	73.07	70.69
$\lvert\nabla\langle\theta\rangle\rvert$	–	–	0.01	0.03	0.26	0.41

The polar angle of the vortex center averaged in the axial direction ($\langle\theta\rangle$) (left: anti-clockwise polar angle, right: clockwise). Difference between left and right axial-averaged vortex center angle ($\nabla\langle\theta\rangle$)

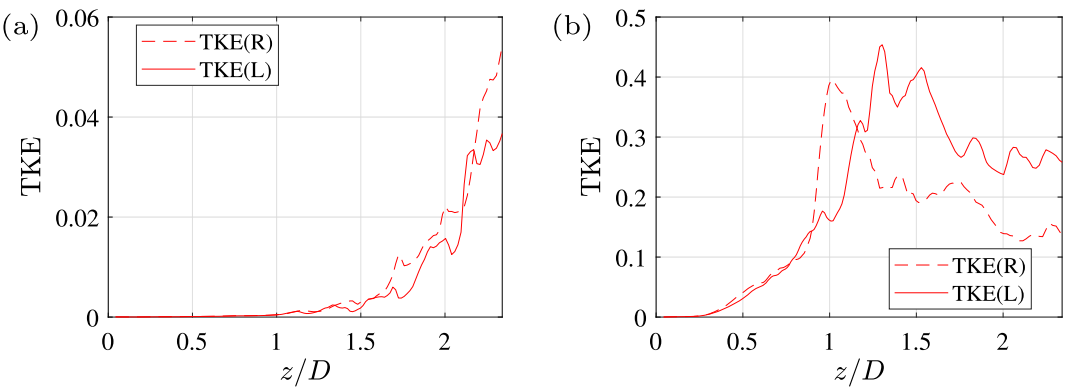

Fig. 10 Turbulent kinetic energy (TKE $= 0.5(\overline{\mathbf{u}'^2})$) along the core of the primary vortex for AoA $=$ **a** 60° and **b** 75°. Dashed and solid lines are for left and right vortices, respectively

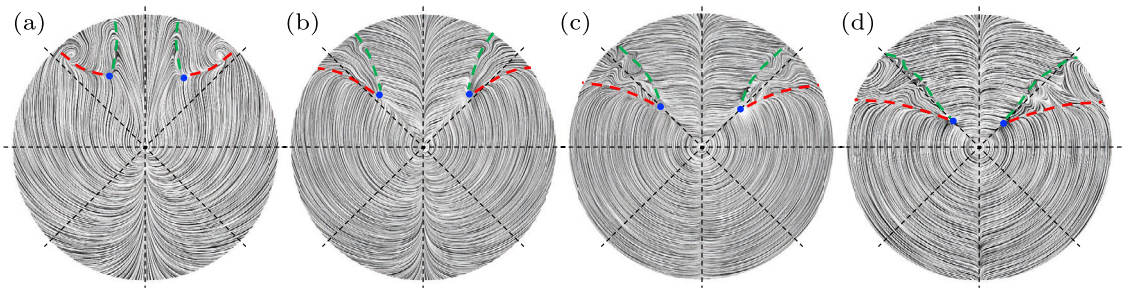

Fig. 11 Limit surface streamlines for AoA = **a** 15°, **b** 30°, **c** 60°, **d** 75°. For detailed caption, see Fig. 5 (color figure online)

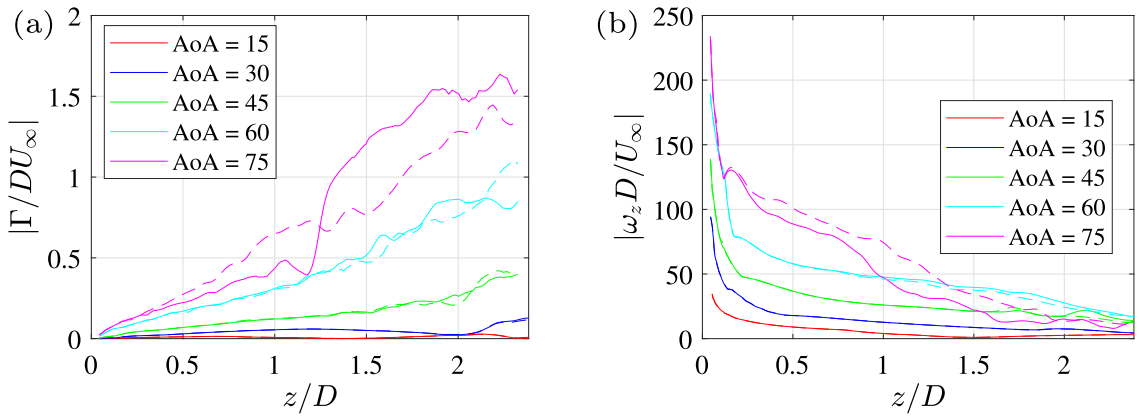

Fig. 12 Circulation around **a** primary vortex and **b** maximum z-component of vorticity inside the primary vortex. Dashed and solid lines are for left and right vortices, respectively

increase. Both of these differences in vortex breakdown and vortex core location are responsible for the asymmetric side force on the body. In Fig. 11, as the AoA increases, the primary separation happens earlier (the red dashed lines move toward the windward side). Since the primary separation point moves toward the windward side, it allows more space for secondary flow to grow on the leeward side of the cone (the separation point moves towards the windward side). For all the AoAs, the primary and secondary separation happens almost at the same location (over a very small region) up to some distance from the tip (blue dots in Fig. 11), and the locations where primary and secondary separation diverge move closer to the tip as the AoA increases.

The time-averaged circulation around the primary vortices is depicted in Fig. 12a. The circulation has been calculated on the xy plane by taking the line integral of the x and y-components of velocity over a selected region for the primary vortex. A discussion has been provided in the "Appendix Section A" about the selection procedure. For AoAs = 30 and 45°, circulation around the primary vortex can be calculated very accurately since the flow remains stable and predictable. At low AoAs, the primary vortex circulation changes linearly along the cone axis. At higher AoAs, the profile does not maintain the linear relationship, and asymmetry started to appear on the circulation profiles. For AoAs = 60 and 75°, the circulation does not maintain the linear relationship after some distance from the tip. Due to the vortex asymmetry, the corresponding curves showing left and right circulations do not overlap for AoA = 75° as shown in Fig. 12a. The asymmetry is observed even before the vortex breakdown which suggests that the vortex breakdown is not solely the source of the asymmetric flow features, an observation consistent with the findings for flow over delta wing by Ma et al. [3]. Figure 12b depicts the maximum z-component of the vorticity inside the primary vortex along the cone axis. For higher AoA, the z-component of vorticity becomes stronger in the wake compared to x and y-components. At low AoAs, the profile shows exponential decay behavior along the axial direction. If the AoA increases, the magnitude of the z-component of the vorticity increases, and hence, the decay starts from a higher value. However, at AoA = 75°, the drop in maximum vorticity does not follow an exponential decay curve. A higher magnitude of z-vorticity leads to higher circulation since the circulation can be represented as the surface integral of the vorticity.

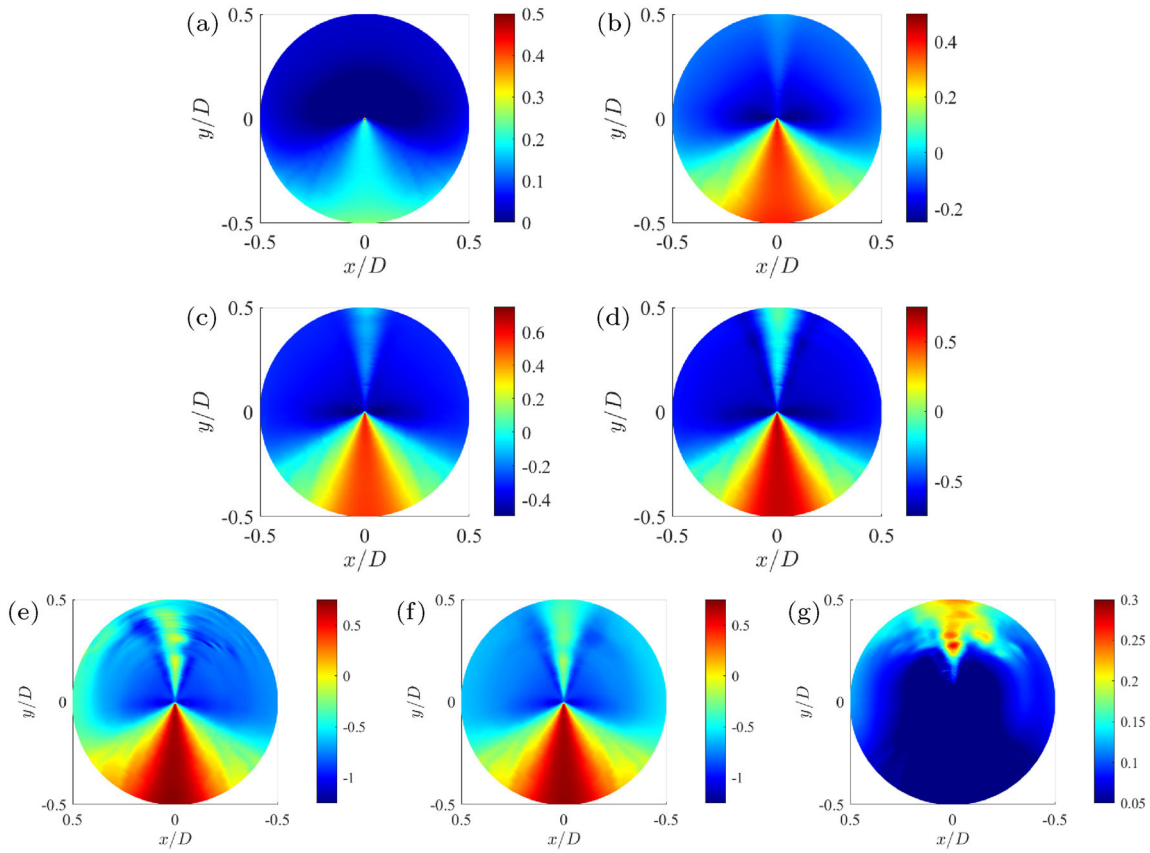

Fig. 13 Average pressure on the surface for AoA = **a** 15°, **b** 30°, **c** 45°, **d** 60°. **e** Instantaneous, **f** average, and **g** standard deviation of the surface pressure for AoA = 75°

3.2.2 Surface pressure and aerodynamic forces

Figure 13 displays the average pressure on the cone surface for AoAs = 15, 30, 45, and 60°, and Fig. 13e–g present the instantaneous, average, and standard deviation of the surface pressure for AoA of 75°, respectively. The major sources of the unsteadiness in a swirling flow are the hydrodynamic instabilities, helical mode instabilities, and vortex breakdown location oscillation [55]. The most unsteady surface pressure was seen for AoA = 75° on the leeward side, whereas, on the windward side, the pressure is mostly steady. The frequency spectrum of the unsteady pressure is shown in Fig. 14 at selected (z/D) distances for three AoAs = 45, 60, and 75°. Only a very low-frequency oscillation is observed for all the cases up to $z/D \approx 1.0$. Higher frequency pressure fluctuations are concentrated on the leeward side of the cone at $z/D \approx 1.85$ location. For AoA = 75° at $z/D \approx 1.85$, the frequencies (fD/U_∞) of the magnitude of 3-−5.5 are bounded within the secondary separation (dashed magenta vertical lines). This separation location has been obtained by identifying the change of sign of the near-wall velocity component projected in the direction of the flow.

For flow over delta wing, the corresponding non-dimensional frequencies (fC/U_∞, where C is chord length) of helical mode instabilities is in the range of 1.76-−3.5 and vortex breakdown location oscillation frequency is in the range of 0.02-−0.1 for a range of angle of attack of 26–37° [55]. For flow over an axisymmetric slender body at a high angle of attack, the dominant frequency (fD/U_∞) of the wake is approximately 0.19 [56]. The dominant rotational frequency of the helical mode of breakdown is reported as 0.2 in Ref. [20]. In this study, at $z/D \approx 1.85$, frequencies—same as the order of helical mode instabilities for delta wing—are observed on pressure fluctuations spectrum for AoA = 45, 60 and 75° both on the windward and a part of the leeward side of the cone. Along with these low-frequency oscillations, for AoA = 75° at $z/D \approx 1.85$ distance, a range of high frequencies from $fD/U_\infty \approx 5.5$-−8.25 can be identified in Fig. 14c which are bounded within the separation point of the secondary flow. These frequencies are only seen in the case with a vortex breakdown region, it can be asserted that they arise from the interaction of small-scale vortical

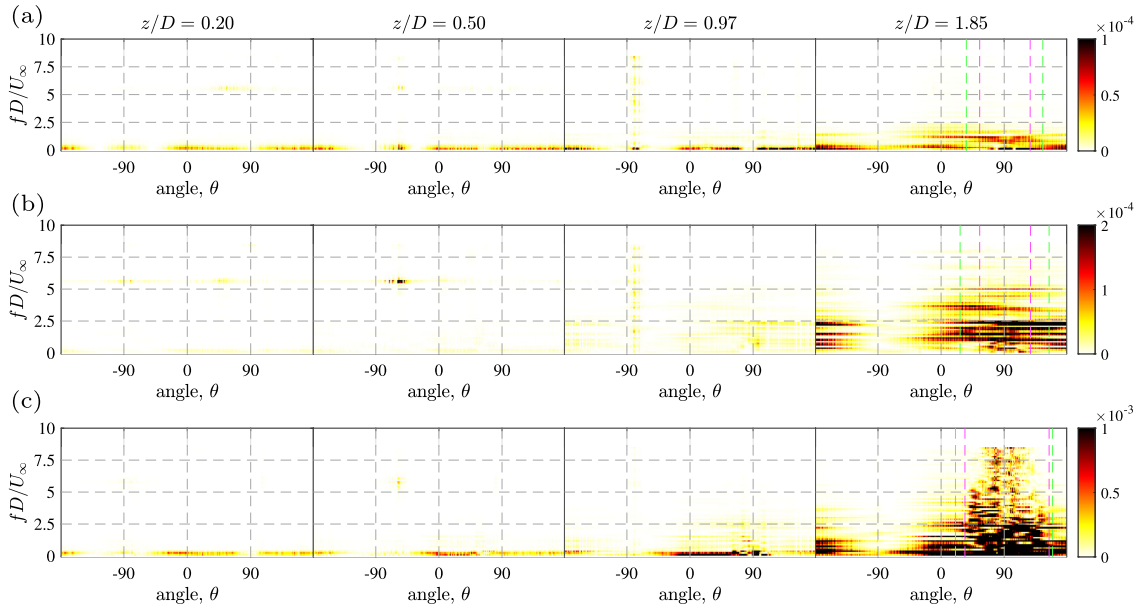

Fig. 14 Frequency content of the surface pressure at $z/D \approx 0.2$, 0.5, 1.0 and 1.85 for AoA = **a** 45, **b** 60 and **c** 75°. The x-axis is the polar angle of the circle on the surface of the cone. The colorbar shows the range of power spectrum density (PSD)

structures (originating from the vortex breakdown) and the secondary vorticity. Please note that the frequencies associated with hydrodynamic instabilities are in the range of $fC/U_\infty = 6$–30 for delta wing [55]. However, for AoA of 45 and 60°, these frequencies are absent at $z/D = 1.85$. Since the vortex breakdown occurs further downstream of this point, it reconfirms that these high frequencies originate from the aerodynamic instabilities associated with the vortex breakdown.

The time-averaged local forces acting on the body are shown in Fig. 15, where the forces are scaled by the local length scale. The following equation calculates all three components of the local forces.

$$c_{\mathrm{D,L,S}} = \frac{dF_{\mathrm{D,L,S}}}{0.5\rho U_\infty^2 D_{\mathrm{L}}}, \tag{4}$$

where dF is the force per unit length along the cone axis and can be either the drag (dF_{D}), lift (dF_{L}), or side force (dF_{S}). The local diameter along the cone axis, D_{L} is employed in the denominator of Eq. 4. The total forces are normalized using the base diameter of the cone as follows

$$C_{\mathrm{D,L,S}} = \frac{F_{\mathrm{D,L,S}}}{0.5\rho U_\infty^2 D^2}, \tag{5}$$

where $F_{\mathrm{D,L,S}}$ refers to the the total forces. For AoA = 30, 45, 60, and 75°, the local lift has a gradual decrease along the cone axis in Fig. 15b–e. In Fig. 15d, even though the time-averaged local side force is almost zero, significant oscillations have been observed near the base which is shown by the dotted lines. At AoA = 75°, the local side force gradually increases in the axial direction, and local drag is higher than the lift along the whole length of the cone.

The total time-averaged side force, drag, and lift are shown in Fig. 16a for all cases. The range of fluctuations (maximum and minimum value) is shown by the dotted lines. Both the lift and drag increase as the AoA increases. The lift is higher than the drag at low angles of attack. The lift reaches its peak at AoA = 60°. As soon as the AoA crosses 60° (where drag and lift are almost the same), the drag overcomes the lift. At 45 and 60° AoA, even though a small instantaneous side force has been observed (dotted blue lines in Fig. 16a), the time-averaged side force is almost zero. However, at AoA = 75°, a relatively large side force is seen in the time-averaged curve in Fig. 16a. From AoA = 15° to 30°, the side force always stays zero. With artificial imperfections, Degani [34] observed that the side force started to appear at AoA = 50° which closely matches our results.

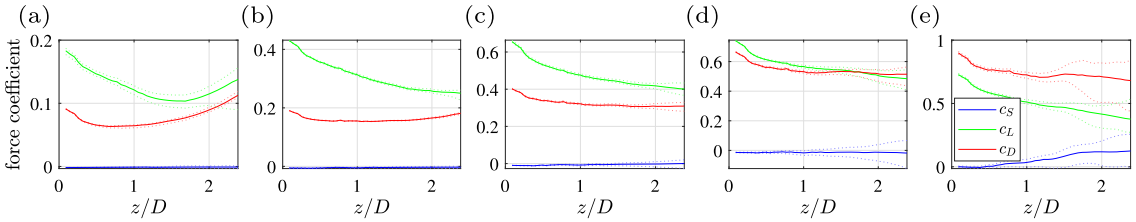

Fig. 15 Local drag, lift, and side-force (normalized by local surface area) for AoA = **a** 15°, **b** 30°, **c** 45° **d** 60° and **e** 75°. The dotted lines show the range of fluctuations of the forces

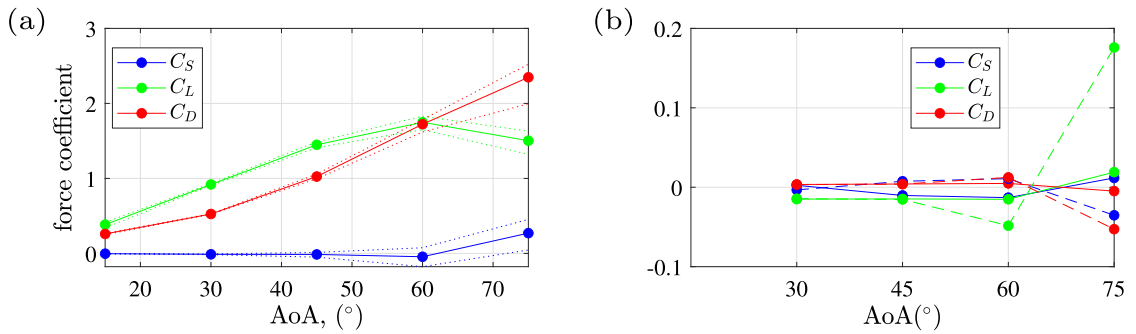

Fig. 16 **a** Total time-averaged side force, drag, and lift for different AoA (the dotted line shows the range of fluctuations). **b** Force coefficient ($F_i/(0.5\rho U_\infty^2 D^2)$ described in Eq. 6 for the zone bounded by the primary vortex. Dashed and solid lines are for left and right vortices, respectively

The aerodynamic force contribution from the primary vortex can be quantified as follows [57,58],

$$F_i = \int_{V_P} (\mathbf{u} \times \boldsymbol{\omega}) \cdot \nabla \phi_i \, \mathrm{d}V_P \tag{6}$$

where V_P is fluid volume bounded by the primary vortex and ϕ_i is the auxiliary potential in i-th direction. A detailed description of the procedure to obtain this force is provided in "Appendix B." Figure 17 provides a qualitative description of force contributed by the primary vortex onto the side force, lift and drag where the values of $(\boldsymbol{u} \times \boldsymbol{\omega}) \cdot \nabla \phi_i \, \mathrm{d}V$ are shown on the different helicity isosurfaces. For side forces at AoA = 45°, the force from the left vortex is neutralized by the force of the right vortex (equal and opposite distribution of the red and blue zone on both sides). However, at AoA = 75°, the counterbalance was not possible because of the flow asymmetry which results in a net side force. At AoA = 45°, the isosurface of the lift has a darker color than the drag which means the primary vortex has more influence on the lift at this AoA. On the other hand, at AoA = 75°, the opposite behavior has been observed, i.e., contribution of $(\boldsymbol{u} \times \boldsymbol{\omega}) \cdot \nabla \phi_i$ on the drag increases. With the increment of AoA, the reduction in lift contribution and rise in drag contribution explain the drop in lift in Fig. 16a from 60° to 75°. At very high AoA, the primary vortex becomes the driving factor for the side forces and partially contributes to the variation of lift and drag.

The aerodynamic force that is coming from the primary vortex (zone identified in Fig. 18) is quantified in Fig. 16b. Time-averaged quantity $(\overline{\boldsymbol{u} \times \boldsymbol{\omega}})$ are used for calculating the forces. The primary vortex is responsible for almost 40% of the total side force acting on the body at AoA = 75°. Among all three forces, if compared to the corresponding total force, the drag is least impacted by the changes in the primary vortex. However, the primary vortex provides approximately 13% of the total lift at AoA = 75°.

4 Conclusion

The vortex dynamics in the wake of an axisymmetric cone are studied and the effects of angle of attack (AoA) on the vortex formation, symmetry breaking of the wake, surface forces, and unsteady pressure on the surface of the cone are quantified for a wide range of AoAs from 15° to 75°.

For flow over axisymmetric bodies, the wake is characterized by two major vortices: primary and secondary vorticity. Helical vortices, spiraling around the core of the primary vortex, were observed at the angle of attack

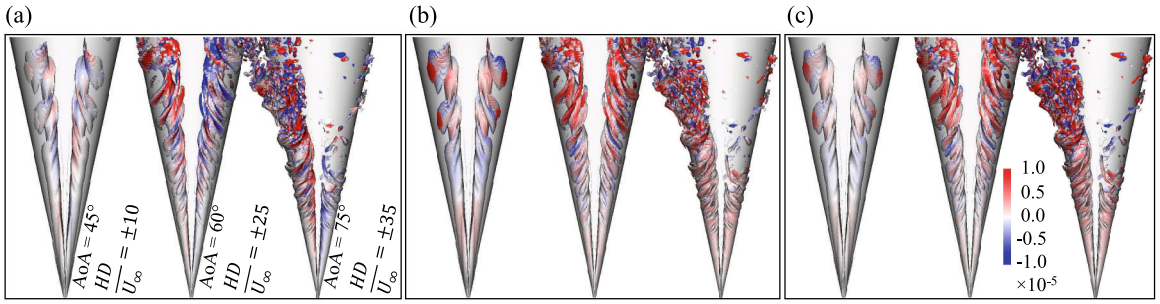

Fig. 17 Instantaneous helicity isosurfaces are extracted at $HD/U_\infty^2 = \pm 10, \pm 25$ and ± 35 for AoA $= 45°, 60°$ and $75°$, respectively. The color is showing the value of $(\boldsymbol{u} \times \boldsymbol{\omega}) \cdot \nabla \phi_i \, dV$ calculated based on the instantaneous flow field where **a** side force ($i = 1$), **b** lift ($i = 2$) and **c** drag ($i = 3$) (color figure online)

of 45°. This vortical structure is generated from the zone between primary and secondary separation. At a sufficiently high AoA, the vortex breakdown phenomenon is observed where the primary vortex disintegrates into small-scale vortical structures without any distinct vortex core. As expected, the degree of swirl plays an important role in the vortex breakdown. The helical vortex also takes part in the vortex breakdown and promotes the double-helix mode of the vortex breakdown mechanism. The cone wake becomes asymmetric at high AoA which is also independent of the vortex breakdown. High-frequency surface pressure fluctuations (originating from vortex breakdown instabilities) have been observed only on the leeward side for high AoA. The side forces start to appear around AoA $= 60°$; coincidentally, at the same angle, the drag force starts to overcome the lift. At AoA $= 75°$, any changes in the side force, drag, and lift are governed by the forces coming from the primary vortex. The main source of asymmetric side force is the asymmetry in the primary vortex.

This study also explains how the flow field forms over the axisymmetric body and how the flow evolves following gradual changes in the body shape. The asymmetric forces result from an asymmetric vortex structure in the wake of the body which itself is a manifestation of vortex-body and vortex-vortex interactions around the cone. Given the tight connection between the wake of axisymmetric bodies and the geometry of the system, further studies are required to investigate the formation and subsequent dynamics of vortical structures in other axisymmetric forebodies and forebody-afterbody configurations such as ogive, cone-cylinder. and ogive-cylinder bodies.

Acknowledgements This study is supported by the U.S. Army Research Office (ARO) Grant number W911NF-18-1-0462 and Defense Advanced Research Projects Agency (DARPA) through Grant number D19AP00035.

Declarations

Conflict of interest The authors declare that they have no competing interests.

Authors' contribution KS and RK conceptualized the study. AS developed the model, conducted the simulations, post-process the results, and prepared the figures. AS and KS analyzed the results and wrote the main manuscript text. All authors reviewed the manuscript.

Data availability The datasets generated during and/or analyzed during the current study are available from the corresponding author upon reasonable request.

Appendix A Identification procedure of the primary and secondary vorticity

The selected region and the location of the core of the vortex have been evaluated from the average flow field data. The velocity gradient eigenmodes are found to be insufficient for identifying the vortex core once the vortex breakdown happens. First, an anisotropic Gaussian filter is applied to remove any small-scale structures. Based on the spatial characteristics of the small-scale vortical structures in the flow, the size and strength of the filter are determined [59]. This filtered field allows systematic identification of the primary vortex core. The selected points were obtained by using user-defined threshold values (changes along the axis of the primary

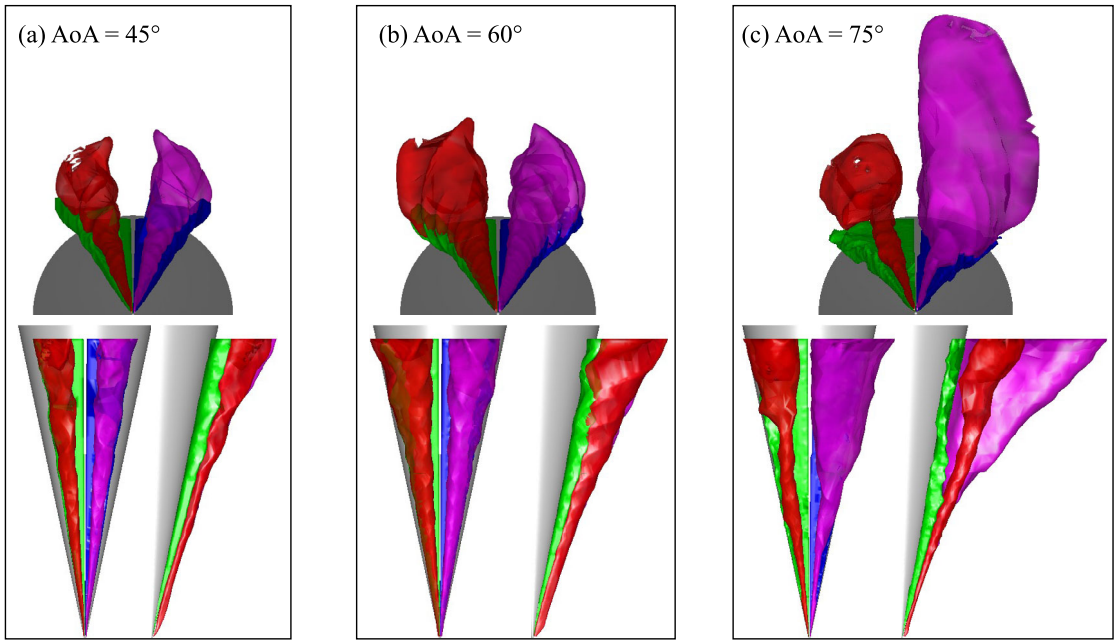

Fig. 18 Zone identified for primary and secondary vorticity for different AoAs

vortex core) for helicity and vorticity. A procedure has also been applied for the identification of the zone for the secondary vorticity. If a point on the left of the domain has vorticity opposite the primary vorticity, the radial distance is less than the center of the primary vortex, and situated on the left side of the domain (i.e., $x < 0$), that point is considered in the region of the left secondary vorticity. The zones that are identified by the algorithm discussed above is shown in Fig. 18.

Appendix B Partitioning of the surface force

According to Ref. [57,58,60], for fluid of volume (V) around an immersed fixed object with the surface (S_0), multiplying the Navier–Stokes equations by $\nabla\phi$ yields

$$-\int_{S_0} P\boldsymbol{n}\cdot\nabla\phi\,\mathrm{d}A = -\rho\int_V(\boldsymbol{u}\times\boldsymbol{\omega})\cdot\nabla\phi\,\mathrm{d}V + \mu\int_{S_0}(\boldsymbol{n}\times\boldsymbol{\omega})\cdot\nabla\phi\,\mathrm{d}A \tag{B1}$$

where, $\boldsymbol{n}$, ϕ, $\boldsymbol{\omega}$ and μ are the unit normal pointing outward on the surface (S_0), auxiliary potential, vorticity, and dynamic viscosity, respectively. Isolating the second term on the right-hand side, the vortex force on a stationary immersed body with a selected fluid volume V bounded by the surface S can be represented as

$$F_i = \int_V(\boldsymbol{u}\times\boldsymbol{\omega})\cdot\nabla\phi_i\;\mathrm{d}V \tag{B2}$$

where ϕ_i is the auxiliary potential governed by the following equations and boundary conditions.

$$\nabla^2\phi_i = 0 \tag{B3}$$

and boundary conditions for ϕ is

$$\nabla\phi_i\cdot\boldsymbol{n} = \begin{cases} n_i & \text{(on body surface } S\text{)} \\ 0 & \text{(on outer boundary } \Sigma\text{)} \end{cases} \tag{B4}$$

where n_i is the i component of the unit normal pointing outward on the surface S, and Σ is the far-field boundary.

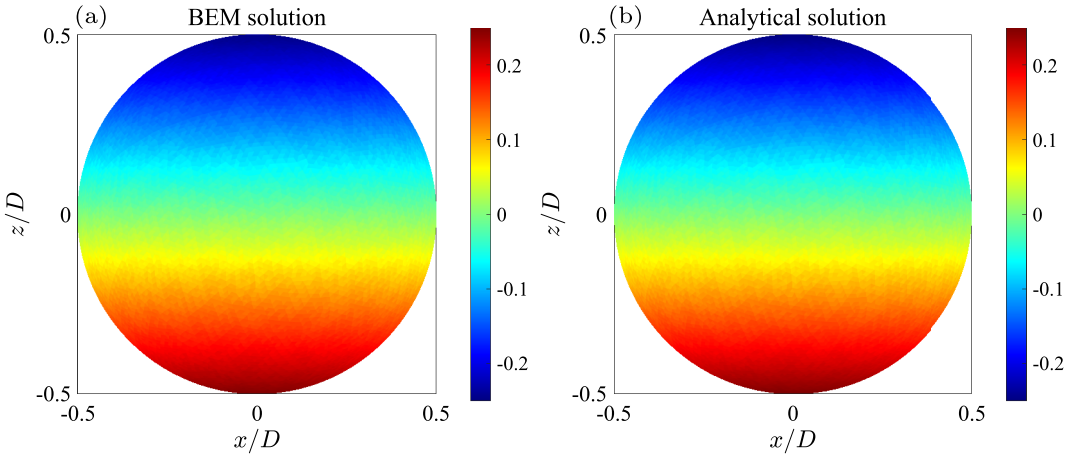

Fig. 19 Auxiliary potential function (ϕ) on the surface of a sphere **a** BEM and **b** analytical solution

B.1 Boundary element method (BEM) for solving auxiliary potential function

The governing Laplace's equation for auxiliary potential function can be solved for any arbitrary surface by boundary element method (BEM). The Green's functions of Laplace's equation constitute a special class of harmonic functions that are singular at an arbitrary point x_0. By definition, Green's function satisfies the singularly forced Laplace's equation

$$\nabla^2 G(\boldsymbol{x}, \boldsymbol{x}_0) + \delta(\boldsymbol{x}, \boldsymbol{x}_0) = 0 \tag{B5}$$

By applying Green's second identity $\nabla \cdot (g\nabla\phi - \phi\nabla g) = 0$ for a non-singular harmonic function $\phi(x)$ and using a Green's function $G(\boldsymbol{x}, \boldsymbol{x}_0)$ in place of $g(x)$, and using the above definition, we obtain

$$\phi(x)\,\delta(\boldsymbol{x}, \boldsymbol{x}_0) = \nabla \cdot [\, G(\boldsymbol{x}, \boldsymbol{x}_0)\nabla\phi(\boldsymbol{x}) - \phi(\boldsymbol{x})\nabla G(\boldsymbol{x}, \boldsymbol{x}_0)\,] = 0 \tag{B6}$$

We can select a control volume V bounded by a closed surface or a collection of surfaces denoted by C. When the pole of Green's function x_0 is placed outside V, the left-hand side of the above equation is non-singular throughout V. Integrating both sides of the equation over V, and using the divergence theorem, we find

$$\int_C [\, G(\boldsymbol{x}, \boldsymbol{x}_0)\nabla\phi(\boldsymbol{x}) - \phi(\boldsymbol{x})\nabla G(\boldsymbol{x}, \boldsymbol{x}_0)\,] \cdot \boldsymbol{n}\, \mathrm{d}S = 0 \tag{B7}$$

where dS is the differential area on C. In contrast, when x_0 is placed inside V, the left-hand side exhibits a singularity at the point x_0. Using the distinctive properties of the delta function to perform the integration, we find

$$\phi(\boldsymbol{x}_0) = -\int_C G(\boldsymbol{x}, \boldsymbol{x}_0)\,[\,\boldsymbol{n} \cdot \nabla\phi(\boldsymbol{x})]\,\mathrm{d}S + \int_C \phi(\boldsymbol{x})\,[\,\boldsymbol{n} \cdot \nabla G(\boldsymbol{x}, \boldsymbol{x}_0)]\,\mathrm{d}S \tag{B8}$$

where the unit normal vector $\boldsymbol{n}$ points into the control area enclosed by C. Above equation provides us with a boundary-integral representation of a harmonic function in terms of the boundary values and the boundary distribution of the normal derivative of the harmonic function. A similar approach can be made if the point x_0 approaches the surface C. To compute the value of $\phi(x)$ at a particular point x_0 located on a selected control area, we can evaluate the two boundary integrals on the right-hand side of the last equation and solve the first type kernel equation for $\phi(x_0)$.

B.1.1 Validation of BEM

To verify the solution convergence of the BEM method described above, the results obtained in the BEM method are compared with the analytical solutions (obtained by the equation below in the spherical coordinate system) to Laplace's equation for potential flow over a sphere in the z-direction.

$$\phi = -\frac{U_\infty a^3 \cos\theta}{2r^2}, r \geq a \tag{B9}$$

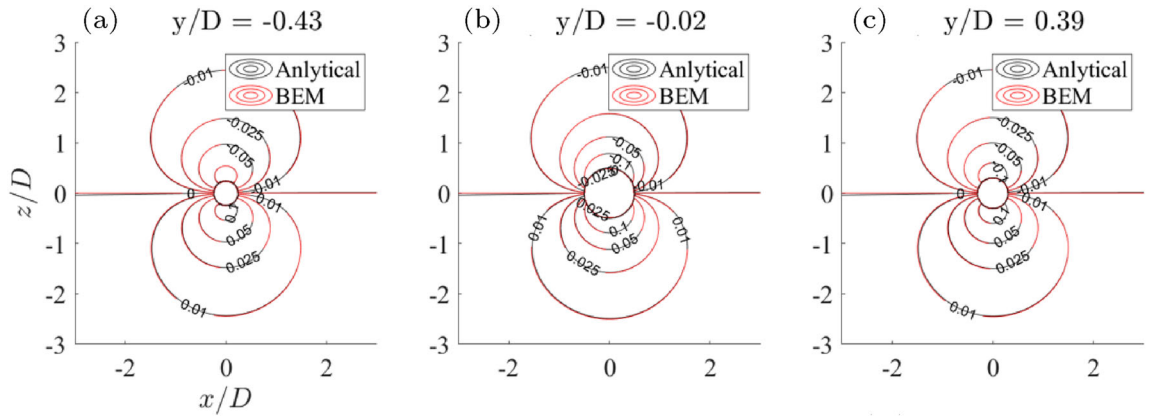

Fig. 20 Comparison of auxiliary potential function (ϕ) in the domain for BEM and analytical solution

where a is the radius of the sphere. Figure 19 shows both the analytical and BEM solution of the auxiliary function on the surface of the sphere.

The contour lines of the analytical solution and the BEM solution of ϕ inside the domain are shown in Fig. 20.

References

1. Mitchell, A.M., Morton, S.A., Forsythe, J.R., Cummings, R.M.: Analysis of delta-wing vortical substructures using detached-eddy simulation. AIAA J. **44**(5), 964–972 (2006)
2. Sun, D., Li, Q., Zhang, H.: Detached-eddy simulations on massively separated flows over a 76/40 double-delta wing. Aerosp. Sci. Technol. **30**(1), 33–45 (2013)
3. Ma, B.-F., Wang, Z., Gursul, I.: Symmetry breaking and instabilities of conical vortex pairs over slender delta wings. J. Fluid Mech. **832**, 41–72 (2017)
4. Leibovich, S.: The structure of vortex breakdown. Ann. Rev. Fluid Mech. **10**(1), 221–246 (1978)
5. Sarpkaya, T.: Turbulent vortex breakdown. Phys. Fluids **7**(10), 2301–2303 (1995)
6. Lucca-Negro, O., O'doherty, T.: Vortex breakdown: a review. Prog. Energy Combust. Sci. **27**(4), 431–481 (2001)
7. Hall, M.: Vortex breakdown. Ann. Rev. Fluid Mech. **4**(1), 195–218 (1972)
8. Escudier, M.: Vortex breakdown: observations and explanations. Prog. Aerosp. Sci. **25**(2), 189–229 (1988)
9. Delery, J.M.: Aspects of vortex breakdown. Prog. Aerosp. Sci. **30**(1), 1–59 (1994)
10. Zilliac, G., Degani, D., Tobak, M.: Asymmetric vortices on a slender body of revolution. AIAA J. **29**(5), 667–675 (1991)
11. Reding, J.P., Ericsson, L.E.: Maximum side forces and associated yawing moments on slender bodies. J. Spacecraft Rockets **17**(6), 515–521 (1980)
12. Hunt, B.: Asymmetric vortex forces and wakes on slender bodies. In: 9th Atmospheric Flight Mechanics Conference, p. 1336
13. Nelson, R.C., Pelletier, A.: The unsteady aerodynamics of slender wings and aircraft undergoing large amplitude maneuvers. Prog. Aerosp. Sci. **39**(2–3), 185–248 (2003)
14. Allen, H.J., Perkins, E.W.: Characteristics of flow over inclined bodies of revolution. Research Memorandum, NACA, Moffet field, California (1951)
15. Gursul, I.: Recent developments in delta wing aerodynamics. Aeronaut. J. **108**(1087), 437–452 (2004)
16. Gursul, I.: Review of unsteady vortex flows over slender delta wings. J. Aircr. **42**(2), 299–319 (2005)
17. Anderson, J.D.: Fundamentals of Aerodynamics. McGraw-Hill Education, New York (2017)
18. Prasad, A., Williamson, C.H.: The instability of the shear layer separating from a bluff body. J. Fluid Mech. **333**, 375–402 (1997)
19. Rajagopalan, S., Antonia, R.: Flow around a circular cylinder-structure of the near wake shear layer. Exp. Fluids **38**(4), 393–402 (2005)
20. Ruith, M., Chen, P., Meiburg, E., Maxworthy, T.: Three-dimensional vortex breakdown in swirling jets and wakes: direct numerical simulation. J. Fluid Mech. **486**, 331–378 (2003)
21. Lowson, M.: Some experiments with vortex breakdown. Aeronaut. J. **68**(641), 343–346 (1964)
22. Kumar, R., Kumar, R., DeSpirito, J.: Development of vortex asymmetry on a generic projectile configuration. J. Spacecr. Rockets **59**(6), 1885–1903 (2022)
23. Lowson, M., Ponton, A.: Symmetry breaking in vortex flows on conical bodies. AIAA J. **30**(6), 1576–1583 (1992)
24. Kumar, R., Viswanath, P., Ramesh, O.: Nose bluntness for side-force control on circular cones at high incidence. J. Aircr. **42**(5), 1133–1141 (2005)
25. Degani, D., Tobak, M.: Experimental study of controlled tip disturbance effect on flow asymmetry. Phys. Fluids A: Fluid Dyn. **4**(12), 2825–2832 (1992)
26. Taligoski, J., Uzun, A., Kumar, R.: Effect of roll orientation on the vortex asymmetry on a conical forebody. In: 53rd AIAA Aerospace Sciences Meeting, p. 0547 (2015)

27. Guan, X., Xu, C., Wang, Y., Wang, Y.: Influence of nose-perturbation location on behavior of vortical flow around slender body at high incidence. Sci. China Ser. E: Technol. Sci. **52**(7), 1933–1946 (2009)
28. Moskovitz, C., Dejarnette, F., Hall, R.: Effects of surface perturbations on the asymmetric vortex flow over a slender body. In: 26th Aerospace Sciences Meeting, p. 483
29. Zhu, Y., Yuan, H., Lee, C.: Experimental investigations of the initial growth of flow asymmetries over a slender body of revolution at high angles of attack. Phys. Fluids **27**(8), 084103 (2015)
30. Qi, Z., Zong, S., Wang, Y.: Bi-stable asymmetry on a pointed-nosed slender body at a high angle of attack. J. Appl. Phys. **130**(2), 024703 (2021)
31. Levy, Y., Hesselnik, L., Degani, D.: Systematic study of the correlation between geometrical disturbances and flow asymmetries. AIAA J. **34**(4), 772–777 (1996)
32. Tobak, M., Peake, D.J.: Topology of three-dimensional separated flows. Ann. Rev. Fluid Mech. **14**(1), 61–85 (1982)
33. Keener, E.R., Chapman, G.T.: Similarity in vortex asymmetries over slender bodies and wings. AIAA J. **15**(9), 1370–1372 (1977)
34. Degani, D.: Development of nonstationary side forces along a slender body of revolution at incidence. Phys. Rev. Fluids **7**(12), 124101 (2022)
35. Coe Jr, P.L., Chambers, J.R., Letko, W.: Asymmetric lateral-directional characteristics of pointed bodies of revolution at high angles of attack. Technical Report NASA-TN-D-7095, NASA (1972)
36. Washburn, A., Visser, K.: Evolution of vortical structures in the shear-layer of delta wings. https://doi.org/10.2514/6.1994-2317
37. Rozema, W., Kok, J.C., Veldman, A.E., Verstappen, R.W.: Numerical simulation with low artificial dissipation of transitional flow over a delta wing. J. Comput. Phys. **405**, 109182 (2020)
38. Visbal, M.R., Gordnier, R.E.: Origin of computed unsteadiness in the shear layer of delta wings. J. Aircr. **32**(5), 1146–1148 (1995)
39. Honkan, A., Andreopoulos, J.: Instantaneous three-dimensional vorticity measurements in vortical flow over a delta wing. AIAA J. **35**(10), 1612–1620 (1997)
40. Ng, T., Oliver, D.: Leading edge vortex and shear layer instabilities. In: 36th AIAA aerospace sciences meeting and exhibit, p. 313 (1998)
41. Lowson, M., Riley, A., Swales, C.: Flow structure over delta wings. In: 33rd aerospace sciences meeting and exhibit, p. 586 (1995)
42. Riley, A., Lowson, M.: Development of a three-dimensional free shear layer. J. Fluid Mech. **369**, 49–89 (1998)
43. Shahriar, A., Shoele, K.: Vortex interactions in the wake of the axisymmetric body in uniform cross-stream. In: AIAA Scitech 2021 Forum, p. 0026 (2021)
44. Ge, L., Sotiropoulos, F.: A numerical method for solving the 3d unsteady incompressible Navier–Stokes equations in curvilinear domains with complex immersed boundaries. J. Comput. Phys. **225**(2), 1782–1809 (2007)
45. Gilmanov, A., Sotiropoulos, F.: A hybrid cartesian/immersed boundary method for simulating flows with 3d, geometrically complex, moving bodies. J. Comput. Phys. **207**(2), 457–492 (2005)
46. Van Kan, J.: A second-order accurate pressure-correction scheme for viscous incompressible flow. SIAM J. Sci. Stat. Comput. **7**(3), 870–891 (1986)
47. Knoll, D.A., Keyes, D.E.: Jacobian-free Newton–Krylov methods: a survey of approaches and applications. J. Comput. Phys. **193**(2), 357–397 (2004)
48. Mittal, R., Iaccarino, G.: Immersed boundary methods. Annu. Rev. Fluid Mech. **37**, 239–261 (2005)
49. Mittal, R., Dong, H., Bozkurttas, M., Najjar, F., Vargas, A., Von Loebbecke, A.: A versatile sharp interface immersed boundary method for incompressible flows with complex boundaries. J. Comput. Phys. **227**(10), 4825–4852 (2008)
50. Shahriar, A., Shoele, K., Kumar, R.: Aero-thermo-elastic simulation of shock-boundary layer interaction over a compliant surface. In: 2018 fluid dynamics conference, p. 3398 (2018)
51. Mahadevan, S., Rodriguez, J., Kumar, R.: Effect of controlled imperfections on the vortex asymmetry of a conical body. AIAA J. **56**(9), 3460–3477 (2018)
52. Finnicum, D.S., Hanratty, T.J.: Effect of favorable pressure gradients on turbulent boundary layers. AIChE J. **34**(4), 529–540 (1988)
53. Visbal, M., Gordnier, R.: On the structure of the shear layer emanating from a swept leading edge at angle of attack. In: 33rd AIAA fluid dynamics conference and exhibit, p. 4016 (2003)
54. Gordnier, R.E., Visbal, M.R.: Unsteady vortex structure over a delta wing. J. Aircr. **31**(1), 243–248 (1994)
55. Gursul, I., Yang, H.: On fluctuations of vortex breakdown location. Phys. Fluids **7**(1), 229–231 (1995)
56. Zeiger, M., Telionis, D., Vlachos, P.: Unsteady separated flows over three-dimensional slender bodies. Prog. Aerosp. Sci. **40**(4–5), 291–320 (2004)
57. Chang, C.-C., Lei, S.-Y.: An analysis of aerodynamic forces on a delta wing. J. Fluid Mech. **316**, 173–196 (1996)
58. Chang, C.-C.: Potential flow and forces for incompressible viscous flow. Proc. R. Soc. Lond. Ser. A: Math. Phys. Sci. **437**(1901), 517–525 (1992)
59. Lee, J., Zaki, T.A.: Detection algorithm for turbulent interfaces and large-scale structures in intermittent flows. Comput. Fluids **175**, 142–158 (2018)
60. Zhang, C., Hedrick, T.L., Mittal, R.: Centripetal acceleration reaction: an effective and robust mechanism for flapping flight in insects. PloS One **10**(8), 0132093 (2015)

Terms and Conditions

Springer Nature journal content, brought to you courtesy of Springer Nature Customer Service Center GmbH (“Springer Nature”).
Springer Nature supports a reasonable amount of sharing of research papers by authors, subscribers and authorised users (“Users”), for small-scale personal, non-commercial use provided that all copyright, trade and service marks and other proprietary notices are maintained. By accessing, sharing, receiving or otherwise using the Springer Nature journal content you agree to these terms of use (“Terms”). For these purposes, Springer Nature considers academic use (by researchers and students) to be non-commercial.
These Terms are supplementary and will apply in addition to any applicable website terms and conditions, a relevant site licence or a personal subscription. These Terms will prevail over any conflict or ambiguity with regards to the relevant terms, a site licence or a personal subscription (to the extent of the conflict or ambiguity only). For Creative Commons-licensed articles, the terms of the Creative Commons license used will apply.
We collect and use personal data to provide access to the Springer Nature journal content. We may also use these personal data internally within ResearchGate and Springer Nature and as agreed share it, in an anonymised way, for purposes of tracking, analysis and reporting. We will not otherwise disclose your personal data outside the ResearchGate or the Springer Nature group of companies unless we have your permission as detailed in the Privacy Policy.
While Users may use the Springer Nature journal content for small scale, personal non-commercial use, it is important to note that Users may not:

1. use such content for the purpose of providing other users with access on a regular or large scale basis or as a means to circumvent access control;
2. use such content where to do so would be considered a criminal or statutory offence in any jurisdiction, or gives rise to civil liability, or is otherwise unlawful;
3. falsely or misleadingly imply or suggest endorsement, approval , sponsorship, or association unless explicitly agreed to by Springer Nature in writing;
4. use bots or other automated methods to access the content or redirect messages
5. override any security feature or exclusionary protocol; or
6. share the content in order to create substitute for Springer Nature products or services or a systematic database of Springer Nature journal content.

In line with the restriction against commercial use, Springer Nature does not permit the creation of a product or service that creates revenue, royalties, rent or income from our content or its inclusion as part of a paid for service or for other commercial gain. Springer Nature journal content cannot be used for inter-library loans and librarians may not upload Springer Nature journal content on a large scale into their, or any other, institutional repository.
These terms of use are reviewed regularly and may be amended at any time. Springer Nature is not obligated to publish any information or content on this website and may remove it or features or functionality at our sole discretion, at any time with or without notice. Springer Nature may revoke this licence to you at any time and remove access to any copies of the Springer Nature journal content which have been saved.
To the fullest extent permitted by law, Springer Nature makes no warranties, representations or guarantees to Users, either express or implied with respect to the Springer nature journal content and all parties disclaim and waive any implied warranties or warranties imposed by law, including merchantability or fitness for any particular purpose.
Please note that these rights do not automatically extend to content, data or other material published by Springer Nature that may be licensed from third parties.
If you would like to use or distribute our Springer Nature journal content to a wider audience or on a regular basis or in any other manner not expressly permitted by these Terms, please contact Springer Nature at

onlineservice@springernature.com